

See discussions, stats, and author profiles for this publication at: <https://www.researchgate.net/publication/221860525>

Hydrogenated TiO₂ Nanotube Arrays for Supercapacitors

ARTICLE in NANO LETTERS · MARCH 2012

Impact Factor: 13.59 · DOI: 10.1021/nl300173j · Source: PubMed

CITATIONS

353

READS

175

7 AUTHORS, INCLUDING:



Xihong Lu

Sun Yat-Sen University

106 PUBLICATIONS 3,410 CITATIONS

SEE PROFILE



Gongming Wang

University of California, Santa Cruz

50 PUBLICATIONS 4,374 CITATIONS

SEE PROFILE



Minghao Yu

Sun Yat-Sen University

47 PUBLICATIONS 2,084 CITATIONS

SEE PROFILE



Yexiang Tong

Sun Yat-Sen University

295 PUBLICATIONS 9,227 CITATIONS

SEE PROFILE

Hydrogenated TiO₂ Nanotube Arrays for Supercapacitors

Xihong Lu,^{†,‡} Gongming Wang,[‡] Teng Zhai,[†] Minghao Yu,[†] Jiayong Gan,[†] Yexiang Tong,^{*,†} and Yat Li^{*,‡}

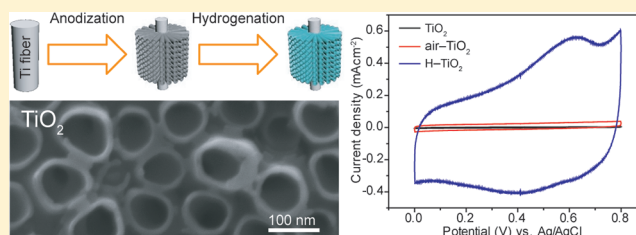
[†]KLGEI of Environment and Energy Chemistry, MOE of the Key Laboratory of Bioinorganic and Synthetic Chemistry, School of Chemistry and Chemical Engineering, Sun Yat-Sen University, Guangzhou 510275, People's Republic of China

[‡]Department of Chemistry and Biochemistry, University of California, Santa Cruz, California 95064 United States

S Supporting Information

ABSTRACT: We report a new and general strategy for improving the capacitive properties of TiO₂ materials for supercapacitors, involving the synthesis of hydrogenated TiO₂ nanotube arrays (NTAs). The hydrogenated TiO₂ (denoted as H-TiO₂) were obtained by calcination of anodized TiO₂ NTAs in hydrogen atmosphere in a range of temperatures between 300 to 600 °C. The H-TiO₂ NTAs prepared at 400 °C yields the largest specific capacitance of 3.24 mF cm⁻² at a scan rate of 100 mV s⁻¹, which is 40 times higher than the capacitance obtained from air-annealed TiO₂ NTAs at the same conditions. Importantly, H-TiO₂ NTAs also show remarkable rate capability with 68% areal capacitance retained when the scan rate increase from 10 to 1000 mV s⁻¹, as well as outstanding long-term cycling stability with only 3.1% reduction of initial specific capacitance after 10 000 cycles. The prominent electrochemical capacitive properties of H-TiO₂ are attributed to the enhanced carrier density and increased density of hydroxyl group on TiO₂ surface, as a result of hydrogenation. Furthermore, we demonstrate that H-TiO₂ NTAs is a good scaffold to support MnO₂ nanoparticles. The capacitor electrodes made by electrochemical deposition of MnO₂ nanoparticles on H-TiO₂ NTAs achieve a remarkable specific capacitance of 912 F g⁻¹ at a scan rate of 10 mV s⁻¹ (based on the mass of MnO₂). The ability to improve the capacitive properties of TiO₂ electrode materials should open up new opportunities for high-performance supercapacitors.

KEYWORDS: Supercapacitors, TiO₂ nanotube arrays, hydrogenation



Supercapacitors, as an energy storage device, have attracted growing interest in recent years.^{1–6} According to the mechanism of charge storage, supercapacitors can be classified as (1) electrical double layer capacitors (EDLCs) that are based on electrostatic charge diffusion and accumulation at the electrode/electrolyte interface; and (2) pseudocapacitors that are dominated by Faradaic reactions on electrode materials.^{7–9} For EDLCs, carbon-based materials are commonly used as electrodes due to their outstanding long-term electrochemical stability as a result of high electrical conductivity and extraordinary chemical stability.^{8,10–12} However, the limited charge accumulation in electrical double layer restricts the specific capacitances of EDLCs in a range of relatively small values between 90 and 250 F g⁻¹. On the contrary, pseudocapacitors made of metal oxides (e.g., RuO₂,^{13,14} NiO,¹⁵ CoO,¹⁶ MnO₂,^{17,18}) or conducting polymers (e.g., polyaniline¹⁹) have achieved substantially higher specific capacitances of 300–1200 F g⁻¹ through surface redox reactions.^{13–19} Nevertheless, pseudocapacitors are usually suffered from the poor electrical conductivity of electrode materials and the irreversibility of Faradaic reactions on electrode surface, which cause gradual loss of capacitance. There are two major approaches to enhance electrochemical capacitance and stability of an electrode. The first approach is to develop nanostructured electrodes with extremely large effective area. Nanotubes,^{8,11–14} nanowires,^{17–19} nano-

sheets,^{16,20} and mesoporous nanostructures²¹ have been studied, and these nanostructures exhibit higher specific capacitances than their bulk counterparts. The second approach is to increase the electrical conductivity of electrodes by mixing them with highly conductive materials. For instance, carbon materials as excellent electrical conductors have been widely used to form composites with metal oxide electrodes.^{22–25} Despite an increase of specific capacitances in carbon-based composites such as NiO/graphene²³ or MnO₂/CNTs²⁴ compared to their metal oxide counterparts, the incorporation of carbon materials does not change the intrinsic properties of metal oxides. It is highly desirable to fundamentally improve the electrical conductivity and pseudocapacitive behavior of metal oxide electrodes.

Highly ordered TiO₂ NTAs hold great promise as supercapacitor electrodes. TiO₂ is known to be chemically stable, and importantly the open-end nanotube structure offers an extremely large, solvated ion accessible surface area. However, the previous reported specific capacitances of TiO₂ NTAs (100–911 μF cm⁻²)^{26–29} are significantly smaller than that obtained from other metal oxides such as MnO₂ and RuO₂.

Received: January 14, 2012

Revised: February 9, 2012

Published: February 24, 2012

The relatively small specific capacitance was attributed to the poor electrochemical activity and poor electrical conductivity of TiO_2 .^{30,31} We hypothesize that hydrogenation of TiO_2 NTAs could address these limitations and thus improve specific capacitance and stability of TiO_2 materials. It was motivated by our recent demonstration that the donor densities of TiO_2 nanostructures are significantly improved by controlled introduction of oxygen vacancy (Ti^{3+} sites) states via thermal treatment in hydrogen atmosphere.³² Furthermore, we anticipate that hydroxyl groups will be introduced on TiO_2 surface during hydrogenation, which could modify the electrochemical activity of TiO_2 and therefore increase its pseudocapacitance, as observed in other electrode materials.^{33–35}

Highly ordered TiO_2 NTAs were fabricated on a Ti fiber (99.7%, 1 mm in diameter) by anodic oxidation in a glycerol aqueous solution containing 0.75% NH_4F , as illustrated in Figure 1a. The as-prepared TiO_2 NTAs were vertically aligned

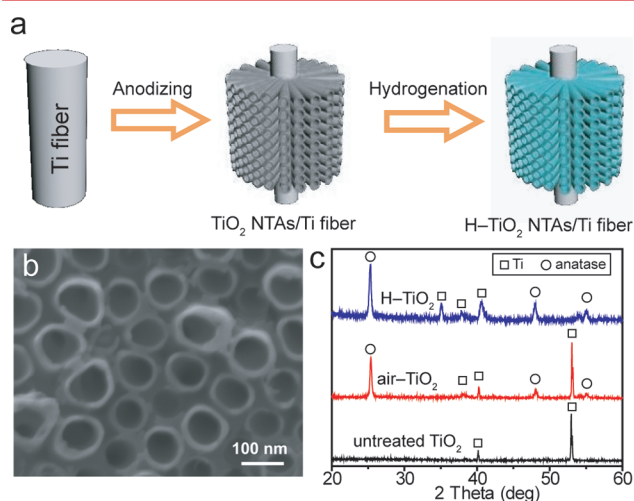


Figure 1. (a) A schematic diagram showing the fabrication of H-TiO₂ NTAs. (b) SEM image of H-TiO₂ NTAs. (c) XRD spectra collected from untreated TiO₂, air-TiO₂, and H-TiO₂ NTAs, respectively. Ti signals are originated from the Ti fiber.

on the Ti fiber (Figure 1b and Figure S1 Supporting Information) with a uniform diameter of ~ 100 nm and a length of ~ 1.2 μm . X-ray diffraction studies reveal that these TiO_2 NTAs are amorphous (Figure 1c). To enhance the mechanical stability and electrical conductivity, the as-prepared TiO_2 NTAs were annealed at 400 °C for 60 min in air (denoted as air-TiO₂) and hydrogen atmosphere (denoted as H-TiO₂), respectively. Scanning electron microscopy (SEM) studies confirm that there are no obvious morphological changes for TiO_2 tubes upon thermal treatment while the amorphous structure transforms to anatase phase (Figure 1c). Furthermore, transmission electron microscopy (TEM) analysis shows that the TiO_2 NTs are polycrystalline structures with inner diameter and wall thickness of about 75 and 20 nm, respectively (Figure S2, Supporting Information). The well-resolved lattice fringes of 0.35 nm are corresponding to the (101) plane of anatase TiO_2 (JCPDF # 21-1272), again confirming the anatase structure.

We performed X-ray photoelectron spectroscopy (XPS) studies to examine the effect of hydrogenation on the chemical composition and oxidation state of TiO_2 nanotubes. Figure 2a shows the normalized Ti 2p core level XPS spectra of air-TiO₂

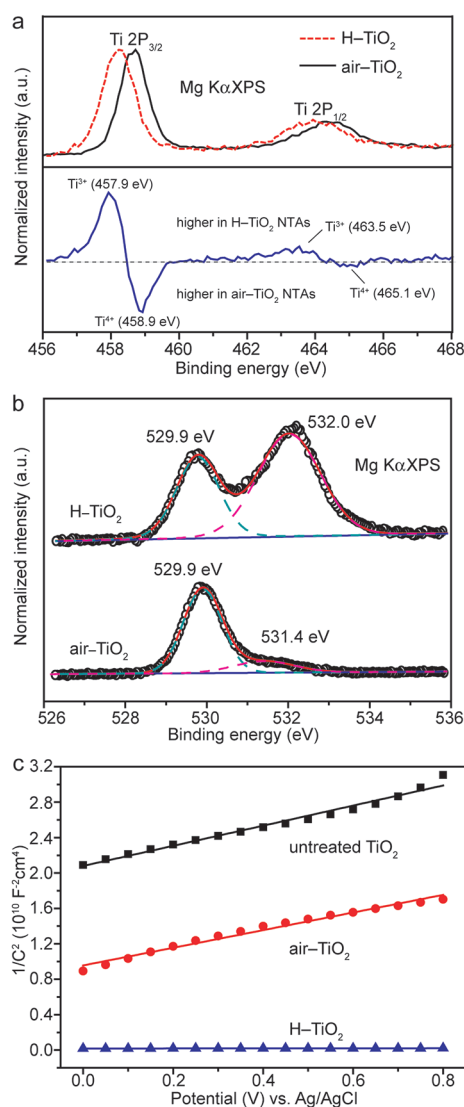


Figure 2. (a) Overlay of normalized Ti 2p core level XPS spectra of air-TiO₂ (black solid curve) and H-TiO₂ NTAs (red dashed curve), together with their difference spectrum (“H-TiO₂” minus “air-TiO₂”). (b) Normalized O 1s core level XPS spectra of air-TiO₂ and H-TiO₂ NTAs. Black circles are the experimental data, which are deconvoluted into two peaks centered at 529.9 eV (green dashed curve) and 531.4–532.0 eV (pink dashed curve). The red curve is the summation of the two deconvoluted peaks. (c) Mott-Schottky plots of the untreated TiO₂, air-TiO₂, and H-TiO₂ NTAs.

and H-TiO₂ samples. Two broad peaks centered at ~ 465.1 and ~ 458.9 eV that correspond to the characteristic Ti 2p_{1/2} and Ti 2p_{3/2} peaks of Ti⁴⁺ are observed for both samples.^{36,37} In comparison to air-TiO₂, the peaks of the H-TiO₂ sample show a negative shift in binding energy, suggesting that they have different bonding environments. By subtracting the normalized Ti 2p spectra of H-TiO₂ with air-TiO₂ sample,³⁸ there are two extra peaks centered at ca. 463.5 and 457.9 eV (Figure 2a). These two peaks are consistent with the characteristic Ti 2p_{1/2} and Ti 2p_{3/2} peaks of Ti³⁺,^{39,40} confirming the presence of Ti³⁺ ions in the H-TiO₂ sample. The result suggests that oxygen vacancies (Ti³⁺ sites) are created in H-TiO₂ nanotubes during hydrogenation. Same conclusion was obtained from Raman analysis (Figure S3, Supporting Information). The characteristic Raman peaks of

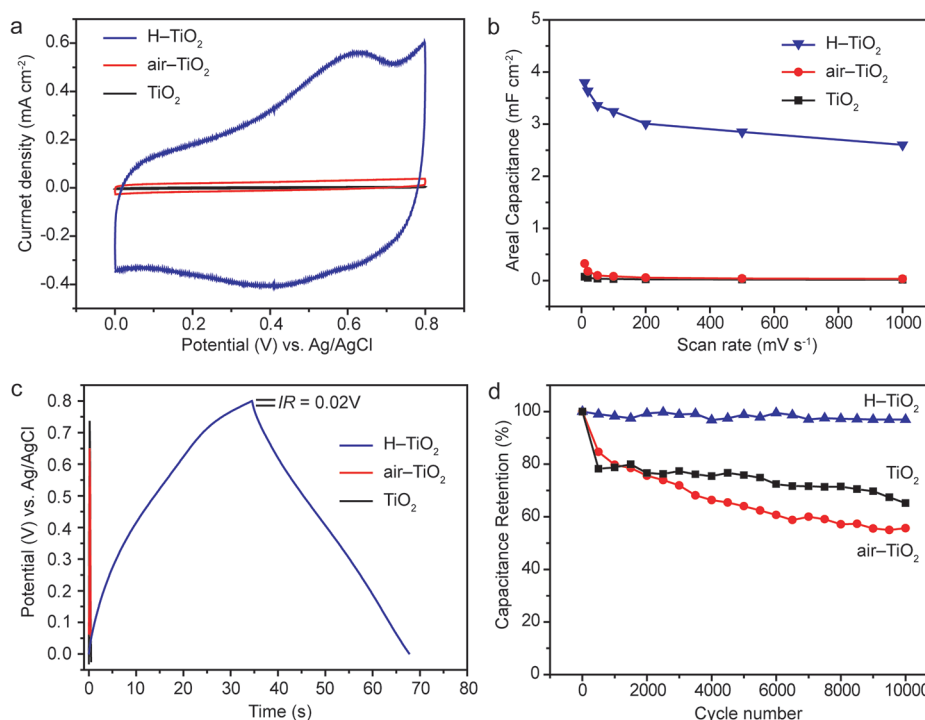


Figure 3. (a) CV curves of the untreated TiO₂, air-TiO₂, and H-TiO₂ NTAs obtained at a scan rate of 100 mV s⁻¹. (b) Areal capacitance of TiO₂ samples measured as a function of scan rate. (c) Galvanostatic charge/discharge curves of TiO₂ samples collected at a current density of 100 μA cm⁻². (d) Cycle performance of TiO₂ samples measured at a scan rate of 100 mV s⁻¹ for 10 000 cycles.

anatase are negatively shifted and broaden for H-TiO₂ sample compared to air-TiO₂ sample, suggesting the increased amount of oxygen vacancies.^{41,42} Figure 2b compares the O 1s core level XPS spectra of air-TiO₂ and H-TiO₂ NTAs. Both samples exhibit the peak of 529.9 eV that corresponds to the characteristic peak of Ti-O-Ti.³⁶ Additional peaks centered at 531.4 and 532.0 eV are attributed to Ti-OH, which has been reported to be located at the binding energy of ~1.5–1.8 eV higher than the peak of Ti-O-Ti.^{17,40} The Ti-OH peak intensity of the H-TiO₂ sample is substantially higher than that of air-TiO₂ sample, indicating the TiO₂ surface are functionalized by hydroxyl groups after hydrogenation.

To investigate the effect of hydrogenation on the electrical properties of TiO₂, electrochemical impedance measurements were conducted on the untreated TiO₂, air-TiO₂, and H-TiO₂ samples. Mott-Schottky plots were generated based on capacitances that were derived from the electrochemical impedance obtained at each potential with 10 kHz frequency in the dark. As shown in Figure 2c, all TiO₂ samples exhibit a positive slope in the Mott-Schottky plots, indicating n-type semiconductor character. Carrier densities of TiO₂ samples were calculated using Mott-Schottky equation

$$N_d = \left(\frac{2}{e_0 \epsilon \epsilon_0} \right) \left[\frac{d \left(\frac{1}{C^2} \right)}{dV} \right]^{-1}$$

where N_d is the donor density, e_0 is the electron charge, ϵ is the dielectric constant of TiO₂ (31 for anatase),⁴³ ϵ_0 is the permittivity of vacuum, and V is the potential applied at the electrode. The carrier densities of the untreated TiO₂, air-TiO₂ and H-TiO₂ NTAs are calculated to be 3.4×10^{20} cm⁻³, $3.6 \times$

10^{20} cm⁻³, and 1.4×10^{23} cm⁻³, respectively. Noteworthy is that the Mott-Schottky equation was derived based on a planar electrode model, and we used the projected area (instead of effective surface area) of the nanotube structures for the calculation that could cause errors in determining the carrier densities. Nevertheless, a qualitative comparison of carrier densities between these samples is valid, as they have similar morphology and surface area. As expected, the untreated TiO₂ sample exhibits the lowest carrier density due to their amorphous structure. Upon annealing in air, the carrier density of TiO₂ increases as a result of improved crystallinity by the formation of anatase. Significantly, hydrogenation leads to a 3 orders of magnitude enhancement in carrier density of TiO₂ NTAs. The increased carrier density can be attributed to the increased oxygen vacancy states, which are known to be electron donors for TiO₂.^{32,44} The formation of oxygen vacancies (Ti³⁺ sites) is supported by the XPS results.

To evaluate the electrochemical properties of TiO₂ and H-TiO₂ NTAs, electrochemical measurements were conducted in a three-electrode electrochemical cell with a graphite rod counter electrode and an Ag/AgCl reference electrode in 0.5 M Na₂SO₄ solution. Figure 3a shows the cyclic voltammetric (CV) curves of the untreated TiO₂, air-TiO₂ and H-TiO₂ nanotube-arrayed electrodes collected at the scan rate of 100 mV s⁻¹. In comparison to the untreated TiO₂ and air-TiO₂ samples, H-TiO₂ sample delivers an obvious pseudocapacitive characteristic, which can be attributed to the oxidation/reduction of surface hydroxyl groups.^{33–35} Furthermore, the CV curves of H-TiO₂ NTAs obtained at various scan rates exhibit quasi-rectangular shapes (Figure S4, Supporting Information). The shapes of these CV curves remain unchanged as the scan rate increase from 10 to 1000 mV s⁻¹, indicating good capacitive behavior and high-rate capability of H-TiO₂ NTAs. Figure 3b shows the calculated areal

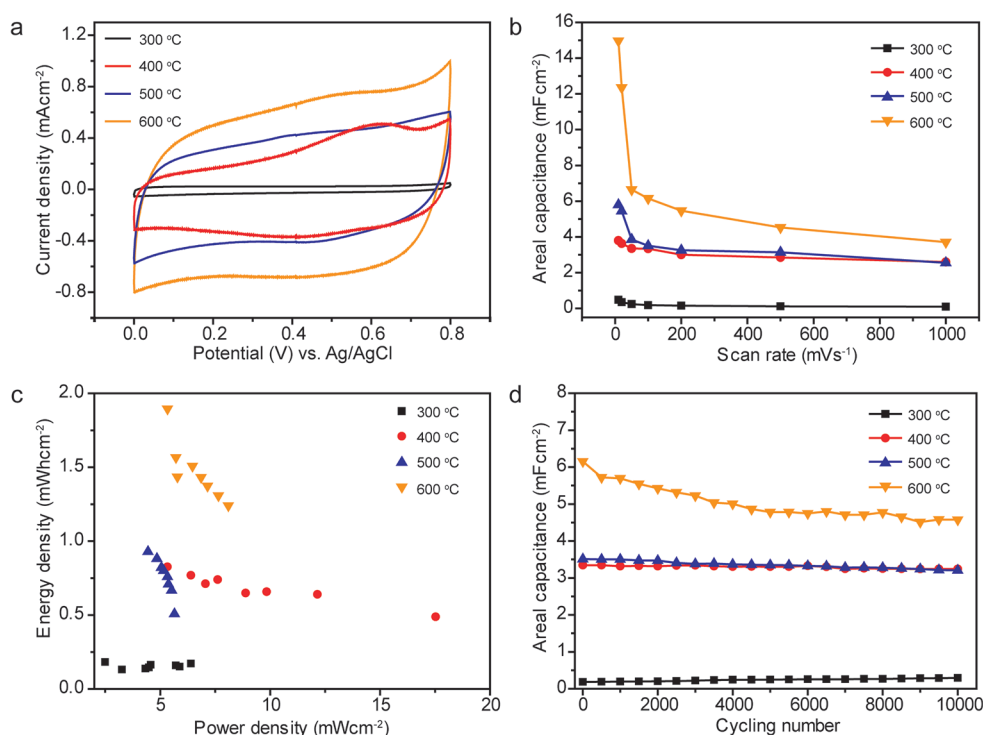


Figure 4. (a) CV curves collected at a scan rate of 100 mV s⁻¹ for H-TiO₂ NTAs hydrogenated at different temperatures. (b) Areal capacitances collected for H-TiO₂ electrodes as a function of scan rate. (c) Ragone plots of H-TiO₂ electrodes obtained at different temperatures. (d) Areal capacitances collected at a scan rate of 100 mV s⁻¹ for H-TiO₂ electrodes for 10 000 cycles.

capacitance of these electrodes as a function of scan rate (detailed calculation see Supporting Information). The areal capacitances of the H-TiO₂ sample is significantly higher than the untreated TiO₂ and air-TiO₂ samples. For instance, the H-TiO₂ electrode achieves an areal capacitance of 3.24 mF cm⁻² at a scan rate of 100 mV s⁻¹, which is a 124- and 40-fold enhancement compared to the untreated TiO₂ (0.026 mF cm⁻²) and air-TiO₂ (0.08 mF cm⁻²) samples. This areal capacitance is also substantially higher than the values recently reported for TiO₂ NTAs (0.538 mF cm⁻²)^{26,28} and TiO₂ nanoparticles (0.12 mF cm⁻²).³⁰ The enhanced electrochemical performance of TiO₂ NTAs can be attributed to two major improvements upon hydrogenation. First, H-TiO₂ samples exhibit improved electrical conductivity (increased carrier density) that facilitates the transport of charge carriers. Second, hydrogenation increases the density of hydroxyl groups on TiO₂ NT surface, and thereby enhances the pseudocapacitance. Moreover, the H-TiO₂ sample shows good rate capacitance. The areal capacitance of the H-TiO₂ sample drops from 3.8 to 2.6 mF cm⁻² with a good retention of 68.4% of the initial capacitance, when the scan rate increases from 10 to 1000 mV s⁻¹. In contrast, the untreated TiO₂ and air-TiO₂ samples retain only 21.2 and 9.5% of the initial capacitance, respectively. The rate capability is related to the rate of ion diffusion (mass transport) in the electrode and the electrode conductivity. Given that the morphologies of these TiO₂ samples are similar, they should have similar ion diffusion rate. Therefore, the improved rate capacitance in H-TiO₂ sample should be due to the enhanced electrical conductivity of electrode.

The electrochemical performance of TiO₂ samples was further studied by galvanostatic charge/discharge measurements. Figure 3c shows the charge/discharge curves of different TiO₂ electrodes collected at a current density of 100 μ A cm⁻².

The charge/discharge curve of the H-TiO₂ electrode is symmetric and substantially prolonged over the untreated TiO₂ and air-TiO₂ electrodes, revealing a good capacitive behavior. Additionally, it shows a small IR drop (0.02 V), again confirming the superior electrical conductivity of the H-TiO₂ electrode. Galvanostatic charge/discharge curves were also collected for the H-TiO₂ sample at various current densities (Figure S6 Supporting Information). A slightly nonlinear sloping potential profile was observed in these charge/discharge curves, indicating Faradaic reactions occur on the H-TiO₂ NT surface,^{29,30,45} which is consistent with the CV results. The areal capacitances of the H-TiO₂ sample derived from the discharging curves measured at different current densities are plotted in Figure S7 (Supporting Information). The areal capacitance of the H-TiO₂ sample measured at the current densities of 100 μ A cm⁻² is calculated to be 4.64 mF cm⁻², which is substantially larger than the values obtained from the untreated TiO₂ and air-TiO₂ samples as well as the previously reported for TiO₂ electrodes^{27,29} at the same current density.

Good cycling stability is one of the most important characteristics for high-performance supercapacitors. TiO₂ electrodes were tested at a scan rate of 100 mV s⁻¹ for 10 000 cycles. As shown in Figure 3d, the capacitances of TiO₂ and air-TiO₂ electrodes drop 34.8 and 44.3%, respectively, after 10 000 cycles. Significantly, the H-TiO₂ electrode exhibits an excellent long-term stability with only 3.1% reduction of capacitance after 10 000 cycles. There is no structural modification of the H-TiO₂ electrode after 10 000 cycles of measurement (Figure S8a, Supporting Information). Additionally, the first and the 10 000th CV curves of the H-TiO₂ sample are more or less the same, indicating the redox reactions on H-TiO₂ electrode surface (pseudocapacitance) are very stable (Figure S8b, Supporting Information). The remarkable

cycling performance for the H-TiO₂ electrode is ascribed to their enhanced electrical conductivity and highly stable surface redox reaction.

The above-mentioned experimental results confirm that the electrochemical performance of TiO₂ is strongly correlated to their electrical conductivity (carrier density). As the carrier density of H-TiO₂ is expected to be depend on the hydrogenation conditions, it motivated us to study the effect of hydrogenation temperature on the structural and electrochemical performance of H-TiO₂ NTAs. As shown in Figure 4a, the capacitive current density of H-TiO₂ electrode increases with the increase of hydrogenation temperature. XRD studies (Figure S9, Supporting Information) reveal that there is no phase change observed for TiO₂ NTAs when the hydrogenation temperature increases from 300 to 600 °C. On the other hand, XPS analysis indicates that the amount of surface hydroxyl groups gradually increases with the increase of hydrogenation temperature (Figure S10, Supporting Information). Mott-Schottky studies reveal a 2 orders of magnitudes enhancement of carrier density in H-TiO₂ sample when the hydrogenation temperature increased from 300 to 400 °C (Figure S11, Supporting Information) possibly due to the improved crystallinity of TiO₂ as well as the creation of oxygen vacancy states. These results suggest that the formation of surface hydroxyl groups and the reduction of TiO₂ are more favorable at high temperature. As expected, the H-TiO₂ sample hydrogenated at 600 °C yields the highest areal capacitance of 14.95 mF cm⁻² at a scan rate of 10 mV s⁻¹ compared to other H-TiO₂ samples prepared at lower temperatures due to the improved electrical conductivity and pseudocapacitance arising from the increased amount of surface hydroxyl groups. To our knowledge, this is the best areal capacitance ever achieved by TiO₂ materials, and it is even comparable to the capacitance obtained from a recently reported Ni-NiO core-shell structure (9 mF cm⁻²).⁴⁶ Moreover, Ragone plots (Figure 4c) show that the H-TiO₂ electrodes achieve the highest power density of 17.5 mW/cm² and the maximum energy density of 1.9 mWh/cm². We also performed cycling measurements to examine the long-term stability of these H-TiO₂ electrodes (Figure 4d). While the H-TiO₂ electrodes obtained between 300 and 500 °C exhibit excellent cycling performance with capacitance drop less than 8% after 10 000 cycles, the H-TiO₂ sample obtained at 600 °C shows a relatively large reduction of ~26% in areal capacitance after 10 000 cycles. The relatively low stability of the 600 °C sample could be due to the hydrogen embrittlement of Ti fiber that degrades the contact between TiO₂ NTs and the fiber substrate. The Ti fiber became fragile and the H-TiO₂ NTAs can be easily peeled off from the Ti fiber after hydrogenation at 600 °C. A possible solution is to prepare TiO₂ NTAs on other substrates such as carbon fabrics that are stable for high-temperature hydrogenation. Investigation of additional substrates is in progress.

In addition to being used as an electrode, the open-end nanotube structure of TiO₂ also enables them to serve as a good support for other capacitive active electrode materials to form composite structures. We used H-TiO₂ NTAs (hydrogenated at 400 °C) to support MnO₂ nanoparticles for supercapacitor electrodes, as MnO₂ is one of the most promising pseudocapacitive materials with high theoretical specific capacitance (~1400 F g⁻¹) but suffer from low electrical conductivity (10⁻⁵–10⁻⁶ S cm⁻¹).^{17,24,47} The MnO₂/H-TiO₂ composites were synthesized by electro-

depositing MnO₂ onto the H-TiO₂ NTs (Experimental Section, Supporting Information). SEM image shows that the H-TiO₂ NTs are completely filled with MnO₂ nanoparticles after 60 s electrodeposition (Figure S12a, Supporting Information). Mn 2p core level XPS spectrum reveals two peaks located at 642.2 and 654.3 eV, which are consistent with the characteristic Mn 2p_{3/2} and Mn 2p_{1/2} binding energies of MnO₂ (Figure S12b, Supporting Information).⁴⁸ It supports the successful preparation of MnO₂. To study the role of TiO₂ support on the electrochemical performance of the composite structure, we also prepared MnO₂/air-TiO₂ NTAs for comparison. In comparison to the MnO₂/air-TiO₂, the CV curve of MnO₂/H-TiO₂ composite exhibits a rectangle-like shape and enhanced capacitive current density (Figure S13, Supporting Information). The areal capacitance of the MnO₂/H-TiO₂ composite is two times larger than that of the MnO₂/air-TiO₂ composite (Figure 5a). Significantly, the MnO₂/H-

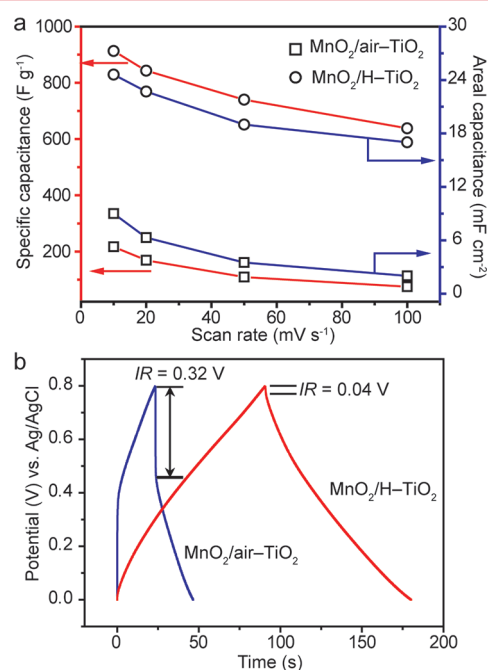


Figure 5. (a) Specific capacitances and areal capacitances of the MnO₂/H-TiO₂ and MnO₂/air-TiO₂ composites measured as a function of scan rate. (b) Galvanostatic charge/discharge curves of the MnO₂/H-TiO₂ and MnO₂/air-TiO₂ NTAs collected at a current density of 200 μA cm⁻².

TiO₂ composite achieves a calculated specific capacitance of 912 F g⁻¹ (based on the mass of MnO₂, Supporting Information) at the scan rate of 10 mV s⁻¹. This value is not only 4 times higher than that of MnO₂/air-TiO₂ sample (217 F g⁻¹), but also higher than the values recently reported for other MnO₂ based composites, such as TiN/MnO₂ nanotubes (~480 F g⁻¹),⁴⁹ SnO₂@MnO₂ nanowires (~540 F g⁻¹),⁵⁰ Zn₂SnO₄@MnO₂ nanorods (~560 F g⁻¹),⁵¹ ZnO@MnO₂ nanorods (~675 F g⁻¹),⁵² and even comparable to CNTs/MnO_x composites (1250 F g⁻¹).⁵³ Furthermore, the MnO₂/H-TiO₂ composite shows good rate capability with a capacitance retention of 69.9% when the scan rate increase from 10 to 100 mV s⁻¹, while it is only 34.6% for the MnO₂/air-TiO₂ composite. These results suggest that MnO₂/H-TiO₂ samples have good electrical conductivity and the charge separation and transport in these highly ordered tubular

structures are efficient. Moreover, the charge/discharge curve of the $\text{MnO}_2/\text{H-TiO}_2$ sample is symmetric with nearly linear slopes and a small IR drop (0.04 V). The small IR drop again indicates the small equivalent series resistance of the H-TiO_2 NTAs.

In summary, we have demonstrated that hydrogenation improves significantly the electrochemical performance of TiO_2 NTAs as electrode materials for supercapacitors. TiO_2 NTAs hydrogenated at 400 °C yields the highest specific capacitances of 3.24 mF cm^{-2} at a scan rate of 100 mV s^{-1} with areal energy density of 0.8 mWh cm^{-2} and power density of 17.5 mW cm^{-2} . Importantly, the H-TiO_2 electrode exhibits excellent long-term stability with only 3.1% reduction of capacitance after 10 000 cycles. The enhancement in capacitance can be attributed to the combined contribution from the improved donor density and the increased density of surface hydroxyl groups. Furthermore, H-TiO_2 NTAs were proved to be excellent supports for other capacitive active materials such as MnO_2 . The $\text{MnO}_2/\text{H-TiO}_2$ composite achieves the highest specific capacitance of 912 F g^{-1} at the scan rate of 10 mV s^{-1} . These findings could open up new opportunities for TiO_2 materials in constructing high-performance supercapacitors as well as other energy storage devices.

■ ASSOCIATED CONTENT

■ Supporting Information

Synthetic and analytical methods, capacitive equations, SEM and TEM images, XPS and XRD spectra, CV and charge/discharge curves, and Mott–Schottky plots. This material is available free of charge via the Internet at <http://pubs.acs.org>.

■ AUTHOR INFORMATION

Corresponding Author

*E-mail: (Y.T.) chedhx@mail.sysu.edu.cn; (Y.L.) yli@chemistry.ucsc.edu.

Notes

The authors declare no competing financial interest.

■ ACKNOWLEDGMENTS

Y.L. acknowledges the financial support of this work in part by NSF (DMR-0847786), faculty startup funds granted by the University of California, Santa Cruz. Y.X.T. acknowledges the financial support of this work by the Natural Science Foundations of China (90923008 and J1103305) and the Natural Science Foundations of Guangdong Province (92510275010 00002). X.H.L. thanks the Academic New Artist Ministry of Education Doctoral Post Graduate (China) for China Scholarship Council financial support.

■ REFERENCES

- (1) Miller, J. R.; Simon, P. *Science* **2008**, 321 (5889), 651–652.
- (2) Liu, D. W.; Garcia, B. B.; Zhang, Q. F.; Guo, Q.; Zhang, Y. Y.; Sepheri, S. S.; Cao, G. Z. *Adv. Funct. Mater.* **2009**, 19 (7), 1015–1023.
- (3) Yu, G.; Hu, L.; Vosgueritchian, M.; Wang, H.; Xie, X.; McDonough, J. R.; Cui, X.; Cui, Y.; Bao, Z. N. *Nano Lett.* **2011**, 11 (7), 2905–2911.
- (4) Yuan, D. S.; Chen, J. X.; Zeng, J. H.; Tan, S. X. *Electrochem. Commun.* **2008**, 10 (7), 1067–1070.
- (5) Chen, L.; Sun, L. J.; Luan, F.; Liang, Y.; Li, Y.; Liu, X. X. *J. Power Sources* **2010**, 195 (11), 3742–3747.
- (6) Bae, J.; Song, M. K.; Park, Y. J.; Kim, J. M.; Liu, M.; Wang, Z. L. *Angew. Chem., Int. Ed.* **2011**, 50 (7), 1683–1687.
- (7) Simon, P.; Gogotsi, Y. *Nat. Mater.* **2008**, 7, 845–854.
- (8) Hua, L. B.; Choi, J. W.; Yang, Y.; Jeong, S.; Mantia, F. L.; Cui, L. F.; Cui, Y. *Proc. Natl. Acad. Sci. U.S.A.* **2009**, 106 (51), 21459–21460.
- (9) Lang, X. Y.; Hirata, A.; Fujita, T.; Chen, M. W. *Nat. Nanotechnol.* **2011**, 6, 232–236.
- (10) Garcia, B. B.; Candelaria, S. L.; Liu, D. W.; Sepheri, S.; Cruz, J. A.; Cao, G. Z. *Renewable Energy* **2011**, 36 (6), 1788–1794.
- (11) Kaempgen, M.; Chan, C. K.; Ma, J.; Cui, Y.; Gruner, G. *Nano Lett.* **2009**, 9 (5), 1872–1876.
- (12) Wang, G.; Ling, Y.; Qian, F.; Yang, X.; Liu, X. X.; Li, Y. J. *Power Sources* **2011**, 196 (11), S209–S214.
- (13) Hu, C. C.; Chang, K. H.; Lin, M. C.; Wu, Y. T. *Nano Lett.* **2006**, 6 (12), 2690–2695.
- (14) Chen, P. C.; Chen, H. T.; Qiu, J.; Zhou, C. W. *Nano Res.* **2010**, 3 (8), 594–603.
- (15) Lee, J. W.; Ahn, T.; Kim, J. H.; Ko, J. M.; Kim, J. D. *Electrochim. Acta* **2011**, 56 (13), 4849–4857.
- (16) Xia, X. H.; Tu, J. P.; Mai, Y. J.; Wang, X. L.; Gu, C. D.; Zhao, X. B. *J. Mater. Chem.* **2011**, 21, 9319–9325.
- (17) Lu, X. H.; Zheng, D. Z.; Zhai, T.; Liu, Z. Q.; Huang, Y. Y.; Xie, S. L.; Tong, Y. X. *Energy Environ. Sci.* **2011**, 4 (8), 2915–2921.
- (18) Xia, H.; Feng, J. K.; Wang, H. L.; Lai, M. O.; Lu, L. J. *Power Sources* **2010**, 195 (13), 4410–4413.
- (19) Yuan, D. S.; Zhou, T. X.; Zhou, S. L.; Zou, W. J.; Mo, S. S.; Xia, N. N. *Electrochem. Commun.* **2011**, 13 (3), 242–246.
- (20) Lei, Z. B.; Christov, N.; Zhao, X. S. *Energy Environ. Sci.* **2011**, 4 (5), 1866–1873.
- (21) Feng, D.; Lv, Y. Y.; Wu, Z. X.; Dou, Y. Q.; Han, L.; Sun, Z. K.; Xia, Y. Y.; Zheng, G. F.; Zhao, D. Y. *J. Am. Chem. Soc.* **2011**, 133 (38), 15148–15156.
- (22) Xu, J. J.; Wang, K.; Zu, S. Z.; Han, B. H.; Wei, Z. X. *ACS Nano* **2010**, 4 (9), 5019–5026.
- (23) Zhao, B.; Song, J. S.; Liu, P.; Xu, W. W.; Fang, T.; Jiao, Z.; Zhang, H. J.; Jiang, Y. J. *J. Mater. Chem.* **2011**, 21 (46), 18792–18798.
- (24) Hu, L. B.; Chen, W.; Xie, X.; Liu, N.; Yang, Y.; Wu, H.; Yao, Y.; Mauro, P.; Alshareef, H. N.; Cui, Y. *ACS Nano* **2011**, 5 (11), 8904–8913.
- (25) Dou, Y. Q.; Zhai, Y. P.; Liu, H. J.; Xia, Y. Y.; Tu, B.; Zhao, D. Y.; Liu, X. X. *J. Power Sources* **2011**, 196 (3), 1608–1614.
- (26) Salari, M.; Aboutalebi, S.; Konstantinov, H. K.; Liu, H. K. *Phys. Chem. Chem. Phys.* **2011**, 13 (11), 5038–5041.
- (27) Xie, Y. B.; Fu, D. G. *Mater. Res. Bull.* **2010**, 45 (5), 628–635.
- (28) Kim, M. S.; Lee, T. W.; Park, J. H. *J. Electrochem. Soc.* **2009**, 156 (7), A584–A588.
- (29) Salari, M.; Konstantinov, K.; Liu, H. K. *J. Mater. Chem.* **2011**, 21 (13), 5128–5133.
- (30) Wang, J.; Polleux, J. L.; Lim, J.; Dunn, B. J. *Phys. Chem. C* **2007**, 111 (40), 14925–14931.
- (31) Fabregat-Santiago, F.; Barea, E. M.; Bisquert, J.; Mor, G. K.; Shankar, K.; Grimes, C. A. *J. Am. Chem. Soc.* **2008**, 130 (34), 11312–11316.
- (32) Wang, G. M.; Wang, H. Y.; Ling, Y. C.; Tang, Y.; Yang, X.; Fitzmorris, R. C.; Wang, C. C.; Zhang, J. Z.; Li, Y. *Nano Lett.* **2011**, 11 (7), 3026–3033.
- (33) Choi, D.; Blomgren, G. E.; Kumta, P. N. *Adv. Mater.* **2006**, 18 (9), 1178–1182.
- (34) Fan, X. Z.; Lu, Y. H.; Xu, H. B.; Kong, X. F.; Wang, J. J. *Mater. Chem.* **2011**, 21, 18753–18760.
- (35) Oda, H.; Yamashita, A.; Minoura, S.; Okamoto, M.; Morimoto, T. *J. Power Sources* **2006**, 158 (2), 1510–1516.
- (36) Chen, X.; Liu, L.; Yu, P. Y.; Mao, S. S. *Science* **2011**, 331 (6018), 746–750.
- (37) Lazarus, M. S.; Sham, T. K. *Chem. Phys. Lett.* **1982**, 92 (6), 670–674.
- (38) Chen, Y. S.; Zhen, K. X.; Liu, X. *Appl. Surf. Sci.* **1998**, 133 (3), 221–224.
- (39) Werfel, F.; Brummer, O. *Phys. Scr.* **1983**, 28 (1), 92–96.
- (40) McCafferty, E.; Wightman, J. P. *Surf. Interface Anal.* **1998**, 26 (8), 549–564.
- (41) Pan, X.; Ma, X. J. *Solid State Chem.* **2004**, 177 (11), 4098–4103.

- (42) Golubovic, A.; Scepanovic, M.; Kremenovic, A.; Askrabic, S.; Berec, V.; Dohevic, M. Z.; Popovic, Z. *J. Sol-Gel Sci. Technol.* **2009**, *49* (3), 311–319.
- (43) Tang, H.; Prasad, K.; Sanjine, R.; Schmid, P. E.; Levy, F. *J. Appl. Phys.* **1994**, *75* (4), 2042–2047.
- (44) Liu, D. W.; Zhang, Y. H.; Xiao, P.; Garcia, B. B.; Zhang, Q. F.; Zhou, X. Y.; Jeong, Y. H.; Cao, G. *Z. Electrochim. Acta* **2009**, *54* (27), 6816–6820.
- (45) Wu, M. S.; Guo, Z. S.; Jow, J. J. *J. Phys. Chem. C* **2010**, *114* (49), 21861–21867.
- (46) Kim, J. H.; Kang, S. H.; Zhu, K.; Kim, J. Y.; Neale, N. R.; Frank, A. J. *Chem. Commun.* **2011**, *47*, 5214–5216.
- (47) Yuan, L. Y.; Lu, X. H.; Xiao, X.; Zhai, T.; Dai, J. J.; Zhang, F. C.; Hu, B.; Wang, X.; Gong, L.; Chen, J.; Hu, C. G.; Tong, Y. X.; Zhou, J.; Wang, Z. L. *ACS Nano* **2012**, *6* (1), 656–661.
- (48) Toupin, M.; Brousse, T.; Bélanger, D. *Chem. Mater.* **2004**, *16* (9), 3184–3190.
- (49) Dong, S. M.; Chen, X.; Gu, L.; Zhou, X. H.; Li, L. F.; Liu, Z. H.; Han, P. X.; Xu, H. X.; Yao, J. H.; Wang, H. B.; Zhang, X. Y.; Shang, C. Q.; Cui, G. L.; Chen, L. Q. *Energy Environ. Sci.* **2011**, *4* (9), 3502–3508.
- (50) Yan, J.; Khoo, E.; Sumboja, A.; Lee, P. S. *ACS Nano* **2010**, *4* (7), 4247–4255.
- (51) Bao, L. H.; Zang, J. F.; Li, X. D. *Nano Lett.* **2011**, *11* (3), 1215–1220.
- (52) He, Y. B.; Li, G. R.; Wang, Z. L.; Su, C. Y.; Tong, Y. X. *Energy Environ. Sci.* **2011**, *4*, 1288–1292.
- (53) Kim, J. H.; Lee, K. H.; Overzet, L. J.; Lee, G. S. *Nano Lett.* **2011**, *11* (7), 2611–2617.